



Cite this: *Phys. Chem. Chem. Phys.*,  
2016, 18, 7715

# Effect of Ag/Au bilayer assisted etching on the strongly enhanced photoluminescence and visible light photocatalysis by Si nanowire arrays†

Ramesh Ghosh,<sup>a</sup> Kenji Imakita,<sup>b</sup> Minoru Fujii<sup>b</sup> and P. K. Giri<sup>\*ac</sup>

We report on the strongly enhanced photoluminescence (PL) and visible light photocatalysis by arrays of vertically aligned single crystalline Si nanowires (NWs) grown by Ag/Au bilayer assisted etching. High resolution FESEM and TEM imaging reveals that the Si NWs are decorated with ultra-small size arbitrary shaped Si nanocrystals (NCs) due to the lateral etching of the NWs. A strong broad band and tunable visible to near-infrared (NIR) photoluminescence (PL) in the range 1.3–2.4 eV are observed for these Si NWs/NCs at room temperature, depending on the etching conditions. Our studies reveal that the visible-NIR PL intensity is about two orders of magnitude higher and it exhibits faster decay dynamics in the bilayer assisted etching case as compared to the Ag or Au single layer etching case. The enhanced PL in the bimetal case is attributed to the longer length and higher density of the Si NWs/NCs, surface plasmon resonance enhanced absorption by residual bimetal NPs and the enhanced radiative recombination rate. Studies on the time evolution of PL spectral features with laser exposure under ambient conditions and laser power dependence reveal that both the quantum confinement of carriers in Si NCs and the nonbridging oxygen hole defects in the SiO<sub>x</sub> layer contribute to the tunable PL. Interestingly, Si NWs grown by Ag/Au bilayer assisted etching exhibit enhanced photocatalytic degradation of methylene blue in comparison to Si NWs grown by single layer Ag or Au assisted etching. The Schottky barrier present between bimetallic NPs and nanoporous Si NWs with Si–H bonds facilitates the photocatalytic activity by efficient separation of photogenerated e–h pairs. Our results demonstrate the superiority of the Si NW array grown by bilayer assisted etching for their cutting edge applications in optoelectronics and environmental cleaning.

Received 20th November 2015,  
Accepted 10th February 2016

DOI: 10.1039/c5cp07161e

www.rsc.org/pccp

## 1. Introduction

Si nanowires (NWs) grown by the metal assisted chemical etching (MACE) method have been attracting a great deal of attention due to their unique properties and diverse range of applications, *e.g.*, in nanoelectronics,<sup>1</sup> optoelectronics,<sup>2</sup> photovoltaics,<sup>3</sup> energy storage,<sup>4</sup> bio-chemical sensors,<sup>5</sup> *etc.* Despite the indirect band gap of bulk Si, Si nanostructures emit light in the UV-visible-near infrared wavelength region depending on the size, doping and surface conditions.<sup>6–18</sup> Efficient visible photoluminescence (PL) has been observed at room temperature (RT) for various forms of nanostructured Si, such as porous Si,<sup>8,9,19</sup> Si NCs<sup>7,10–15,18</sup> and Si NWs.<sup>14,20,21</sup> However, the mechanism of PL from Si NWs is

often debated. While several studies emphasize the effect of quantum confinement (QC) of carriers on the visible PL from Si NWs, a strong influence of defects on the PL has been emphasized in other studies.<sup>8,13,22</sup> Recent studies have shown that Si NCs produced by the side wall etching of Si NWs during metal assisted etching strongly contribute to the visible PL.<sup>7</sup> Si NCs/NWs are often covered with a native oxide layer and the nonbridging oxygen hole center (NBOHC) in the oxide matrix also contributes to the visible PL at RT.<sup>21,23,24</sup> MACE grown Si NWs exhibit high absorption, extremely low reflection and tunable PL in the entire visible-NIR range.<sup>7</sup> Some studies suggest that excitons generated within the nanoporous Si NWs could be energetic enough to drive applicable photoelectrochemical reactions under visible light illumination.<sup>25–28</sup>

During the last few decades, MACE of Si wafers has emerged as a promising and significant tool for rapid production of large area, aligned and well controlled Si NWs and has been recognized as a superior tool over the other well established methods for the production of device quality Si NWs.<sup>7,20,29,30</sup> Mostly, Ag and Au have been used as the noble metal catalysts for the

<sup>a</sup> Department of Physics, Indian Institute of Technology Guwahati, Guwahati-781039, India. E-mail: giri@iitg.ernet.in

<sup>b</sup> Department of Electrical and Electronic Engineering, Graduate School of Engineering, Kobe University, Kobe 657-8501, Japan

<sup>c</sup> Centre for Nanotechnology, Indian Institute of Technology Guwahati, Guwahati-781039, India

† Electronic supplementary information (ESI) available. See DOI: 10.1039/c5cp07161e

growth of Si NWs by MACE. More recently, Ag/Au bilayer metal has been attempted to overcome some of the drawbacks of conventional Ag or Au assisted Si etching for the fabrication of arrays of uniform Si NWs.<sup>31</sup> Since surface conditions of the Si NWs are critical to their electronic and optoelectronic applications, controlling the properties of Si NWs by Ag/Au bilayer assisted MACE grown Si NWs may be a powerful approach to enhance the optoelectronic properties of the Si NWs. Though visible PL and some photocatalytic activity have been reported for Si NWs grown by Ag or Au assisted MACE methods,<sup>7,14,26</sup> to our knowledge, the effect of Ag/Au bilayer assisted growth on the efficient visible-NIR PL and excellent photocatalytic activity of MACE grown Si NWs has not been reported. Comparative studies of the effect of bimetallic NPs and single metal NPs on the morphology of MACE grown Si NWs have not been addressed in detail. MACE grown Si NWs often have residual metal nanoparticles at the bottom of the NWs, which influence the PL efficiency of the NWs by the plasmonic effect. However, the plasmonic effect in the case of Ag/Au bilayer metal may be remarkably different from that of the single metal layer and its effect on the photoluminescence from Si NWs/NCs is worthy of investigation.

In this work, we report on the morphological, structural, photoluminescence and photocatalytic properties of arrays of Si NWs prepared by MACE using the Ag/Au bilayer as the noble metal catalyst. We have investigated the efficacy of the Ag/Au bimetal over conventional Ag or Au metal as the catalyst for the MACE of Si in terms of morphology, PL and photocatalytic properties of the NWs. Self-grown Si NCs of different shapes and sizes are formed on the surface of Si NWs due to the side wall etching of Si NWs that results in porous like Si NWs. We focus on understanding the origin of enhanced visible-NIR PL at RT and visible light photocatalysis from the Si NWs decorated with Si NCs. Time evolution of PL spectra with laser exposure under ambient conditions and laser power dependence reveal the relative contribution of different species in the PL spectra. Time resolved PL studies are carried out to understand the mechanism of enhanced and tunable PL. Further, comparative photocatalytic activities of MACE grown Si NWs using the single layer Ag or Au catalyst with that of the bilayer Ag/Au catalyst are reported for the first time. The origin of the enhanced photocatalytic efficiency of Si NWs grown by bilayer assisted etching is discussed. For the first time, we have demonstrated two efficient but contrasting phenomena of PL and photocatalysis taking place in the same Si NW sample grown by MACE.

## 2. Experimental details

Si NWs were grown from p-type and n-type Si(100) wafers with resistivity 1–10  $\Omega\text{ cm}^{-1}$ . The wafers were first cleaned by the typical Radio Corporation of America (RCA) cleaning process.<sup>7</sup> For etching of the cleaned Si wafers, we used a two-step process. In this process, an ultra-thin layer of metal [Ag (10 nm), Au (2 nm) and Ag (10 nm)/Au (2 nm) bilayer] film was first deposited by thermal evaporation under high vacuum on the Si substrates. In the case of bilayer metal, first the Ag layer

(10 nm) was deposited and subsequently the Au layer (2 nm) was deposited over the Ag layer without breaking the vacuum. These ultra-thin metal layers form interconnected nanostructures on Si substrates leaving an open area for Si etching. Subsequently, all as-deposited substrates were immersed in a solution containing HF and H<sub>2</sub>O<sub>2</sub> (4 : 1 volume ratio) for 5 min at RT. The Ag, Au and Ag/Au bilayer assisted MACE grown samples are named as AgSi, AuSi and AgAuSi, respectively. Samples were prepared for different durations and different HF : H<sub>2</sub>O<sub>2</sub> concentration ratios to monitor changes in morphology and their effect on the PL intensity. The morphology and the structure of the Si NWs were characterized using a field emission scanning electron microscope (FESEM) (Sigma, Zeiss) equipped with an energy-dispersive X-ray spectrometer (EDX) and a transmission electron microscope (TEM) (JEOL-JEM 2010) operated at 200 kV, respectively. For understanding the topography of the metal NP coated Si wafers, we have used atomic force microscopy (AFM) (Agilent-5500) in non-contact mode. For compositional analysis, Fourier transform infrared spectroscopy (FTIR) (Perkin-Elmer, Spectrum BX) and X-ray photoelectron spectroscopy (XPS) measurements were carried out. XPS was carried out using a PHI X-Tool automated photoelectron spectrometer (ULVAC-PHI Inc.) using an Al K $\alpha$  X-ray beam (1486.6 eV) with a beam current of 20 mA. The carbon 1s spectrum was used for the calibration (284.8 eV) of the XPS spectra recorded for various samples.<sup>32</sup> The steady state photoluminescence (PL) spectrum was recorded using a 405 nm diode laser (Cube, Coherent) excitation with the help of a spectrometer (focal length: 30 cm; blaze wavelength: 500 nm) equipped with a cooled charge-coupled device (Princeton Instruments, PIXIS 100B) detector. Each spectrum was corrected for the detector response as a function of wavelength after background subtraction. Raman scattering measurements were carried out with a 514 nm Ar<sup>+</sup> laser excitation using a micro-Raman spectrometer (LabRAM HR-800, Jobin Yvon). Reflectivity measurements were performed using a commercial spectrophotometer (SolidSpec, Shimadzu) equipped with an integrating sphere. Photocatalytic degradation of methylene blue (MB) (1 mg MB in 1000 ml DI water) using Si NWs was performed in a commercial photochemical reactor (Lelesil Innovative Systems, Mumbai). A time programmable visible lamp was used for illuminating the samples up to 200 min with excitation wavelengths 390–730 nm. After every 20 min exposure, 5 ml of MB solution was taken out and UV-vis absorption measurements were carried out using a commercial spectrophotometer (JASCO V-630).

## 3. Results and discussion

### 3.1. Growth and morphology

Studies on the growth mechanism of Si NWs using the two-step MACE are reported by several groups.<sup>7,29,30,33</sup> It has been recognized that during the MACE process, due to lateral etching of Si NWs porous NWs are formed under certain etching conditions and this gives rise to the formation of arbitrary shaped Si NCs on the surface of the Si NWs.<sup>7</sup> The shape and size of the Si NCs

are decided by the size of the pores and intermediate distance between the pores. Note that the surface morphologies of the MACE grown Si NWs are different for different metal catalysts under identical etching conditions. Fig. 1(a–c) shows the FESEM top view images of AgSi, AuSi and AgAuSi, respectively. Fig. 1(d) shows the FESEM cross sectional image of the vertically aligned Si NW array in AgAuSi. It is clear that after 5 min etching, AgSi and AuSi show porous like structures on the Si surface, without having any well-formed Si NWs. In contrast, the AgAuSi shows vertically aligned long Si NWs for the same etching duration. We have performed the growth experiment for a higher etching time (30 min) and observed vertically aligned, long ( $\sim 25 \mu\text{m}$ ) and straight Si NW arrays for AgAuSi, as depicted in Fig. 1(e). Thus, the morphology of the MACE grown Si NWs strongly depends on the nature of the noble metal catalyst. In order to remove the residual metal NPs, the samples were etched in  $\text{HNO}_3$  solution after growth in each case. However,  $\text{HNO}_3$  etching is not able to remove the bilayer metal NPs from the Si NWs due to covering of the Au layer on the Ag layer. The EDX spectra in Fig. 1(f) confirm that the Ag and Au NPs are present on AgAuSi. Fig. 1(g) shows the TEM image of a single Si NW in AgAuSi and it is clear that the bimetal NPs are attached on the surface of the Si NWs during lateral etching. The inset shows a magnified view of the metal NPs trapped in the side wall of Si NWs and the metal NPs are nearly spherical in shape. The TEM image of a single Si NW in Fig. 1(g) confirms that the surface of the Si NW is rough due to the side wall etching and it gives rise to arbitrary shaped Si NCs on the surface of Si NWs, as indicated by the arrows. Fig. 1(h) shows a magnified view of the Si NCs grown on the surface of the Si NWs. The arbitrary shapes of the Si NCs are indicated by

white dashed lines. Note that the average dimension of the Si NCs is  $< 5 \text{ nm}$ . Fig. 1(j) and (k) show the HRTEM lattice image and corresponding IFFT image depicting the high crystallinity of the Si NW as well as Si NCs. The lattice spacing ( $d = 2.95 \text{ \AA}$ ) in Fig. 1(k) confirms that the Si NWs/NCs are single crystalline and are (111) oriented. The reduced  $d$ -spacing ( $2.95 \text{ \AA}$  instead of  $3.11 \text{ \AA}$ ) implies a compressive strain in the lattice, which is due to the anisotropic etching and the native oxide layer present on the Si NW/NC surface.<sup>7</sup> The formation process of porous Si NWs has been discussed by several groups.<sup>30,31,34</sup> Usually, crystal defects and impurities such as dopants in the case of doped Si at the Si surface are thought to serve as nucleation sites for the pore formation. As a result, lower resistivity wafers show higher porosity.<sup>30</sup> Note that in the present study, we have used the Ag/Au bimetal catalyst for Si etching and compared the results with that of the conventional single metal Ag and Au catalysts. In the case of Ag and Au assisted etching for 5 min, porous like structures on the Si surface are formed, while vertically aligned long Si NWs decorated with Si NCs were formed in the case of Ag/Au bimetal assisted etching under the same etching conditions. The conventional Ag or Au assisted Si etching has several drawbacks, *e.g.*, (i) the Ag layer is very unstable in air due to its tendency to become Ag oxide, (ii) the Ag metal undergoes dissolution induced structural failure during Si etching for an extended period of time. The problem becomes significant when the amount of Ag is reduced inside the pores of the Si NWs, which results in the highly porous and nonuniform Si NWs.<sup>31</sup> (iii) Due to the poor cohesion of Au with Si and high etch rate, in the case of pure Au assisted Si etching the Si NWs are not uniform and instead of Si NWs, a porous Si layer is formed.<sup>35</sup> On the other hand, the Ag/Au bilayer metal catalyst allows us to

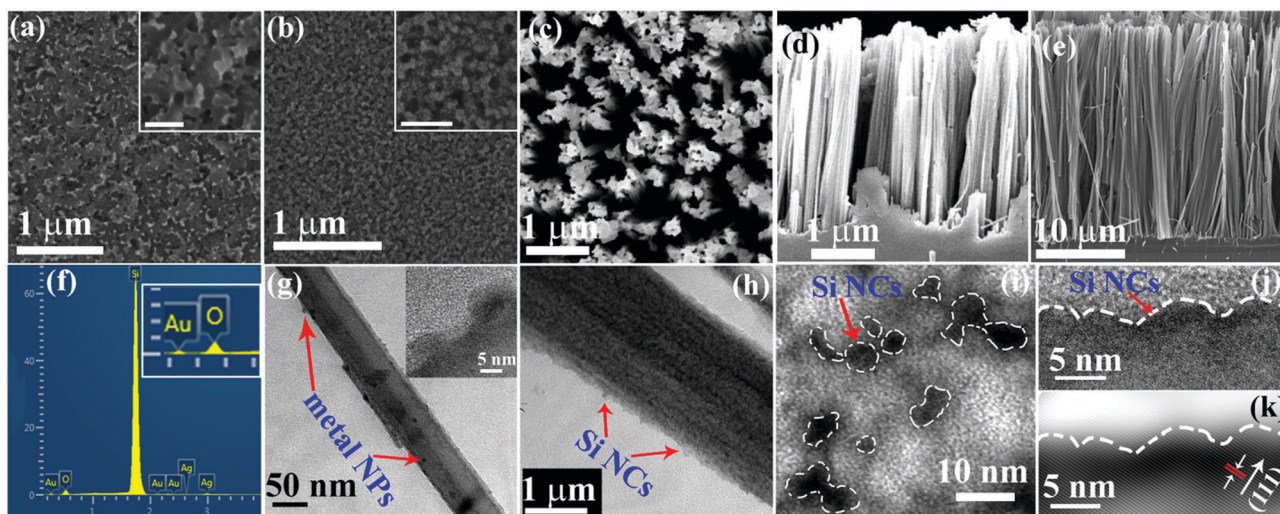


**Fig. 1** FESEM top view images of the samples (a) AgSi, (b) AuSi and (c) AgAuSi, respectively, after 5 min etching. The insets of (a) and (b) show the magnified view of a portion of the corresponding images. The scale bar is  $200 \text{ nm}$  in each case. (d and e) FESEM cross-sectional images of the vertically aligned Si NW array in AgAuSi after etching for 5 min and 30 min, respectively. (f) The corresponding EDX spectrum confirming the presence of the Ag and Au NPs on AgAuSi. The inset shows a magnified view of a portion of the spectrum. (g) The TEM image of a single Si NW showing bimetal NPs on the surface of the Si NW and the inset shows the enlarged view of the bimetal NP–Si NW interface. (h) The TEM image of a single Si NW showing Si NCs due to side wall etching. (i) A higher magnification TEM image showing arbitrary shaped Si NCs (marked by white dashed border). (j and k) The HRTEM image and corresponding IFFT image of the surface protrusions of the Si NW showing single crystalline Si NCs.

overcome the drawbacks of the conventional Ag or Au assisted Si etching. Interestingly, in the case of Ag/Au bilayer assisted etching, Ag nanoparticles (NPs) are sandwiched between the Au layer and Si, which gives rise to the following advantages: (i) Ag is in direct contact with Si and protected by the more stable Au layer, which prevents the Ag layer from oxidation, (ii) Ag plays the role of an etching front, as well as guides the morphology of the following Au layer. The slow etch rate of Ag compared to Au makes the catalyst film stable during prolonged etching; the etching happens only in the vertical direction,<sup>35</sup> (iii) the overlying Au layer protects the dissolution of Ag into etchants and provides mechanical cohesion for the discontinuous underlying Ag layer. Before etching, the morphology and topography of the metal coated Si are checked. Fig. S1(a and b) and (c and d) (ESI†) show the AFM topography images of a 10 nm Ag layer on Si, 10 nm Ag followed by a 2 nm Au layer on Si, respectively, at different magnifications. Fig. S1(e and f) (ESI†) shows the FESEM images of the corresponding Ag and Ag/Au layers. It is found that the Au layer forms isolated Au NPs (average radius 15–25 nm) on the top of the interconnected Ag NPs (average radius 5–10 nm) layer. During the etching, the regions with bimetal NPs form structures that show interesting optical properties of the NWs.

In principle, MACE involves two successive processes: surface nucleation of metal catalysts and anisotropic etching in the vertical direction.<sup>33</sup> With the repetition of these two successive processes, arrays of vertically aligned Si NWs are formed and due to the lateral etching, the surface of Si NWs is decorated with arbitrary shaped ultra small size Si NCs.<sup>6,7,30,36</sup> These Si NCs strongly influence the optical properties of the MACE grown Si NWs.<sup>7</sup>

### 3.2. XPS analysis

In order to investigate the chemical composition and the nature of defects in Si NW/NCs, XPS studies were carried out on AgAuSi. XPS studies confirm that the Si NWs as well as the Si NCs are covered by a native suboxide layer of Si, *i.e.*, SiO<sub>x</sub> (0 < x < 2) layer. Fig. 2(a) shows the Si 2p core-level spectrum of AgAuSi, which exhibits two peaks at ~99.4 eV and ~103.0 eV. These peaks correspond to the neutral Si and its different oxidation states. The 99.4 eV peak corresponds to Si<sup>0</sup> (Si) and the broad 103.0 eV peak corresponds to the combination of Si<sup>3+</sup> (Si<sub>2</sub>O<sub>3</sub>) and Si<sup>4+</sup> (SiO<sub>2</sub>) states.<sup>32,37</sup> XPS analysis thus confirms the presence of the SiO<sub>x</sub> layer on the Si NWs/NCs and this SiO<sub>x</sub> layer is responsible for the compressive strain in the Si NWs/NCs, as revealed from the Raman analysis discussed later. From the O 1s spectrum

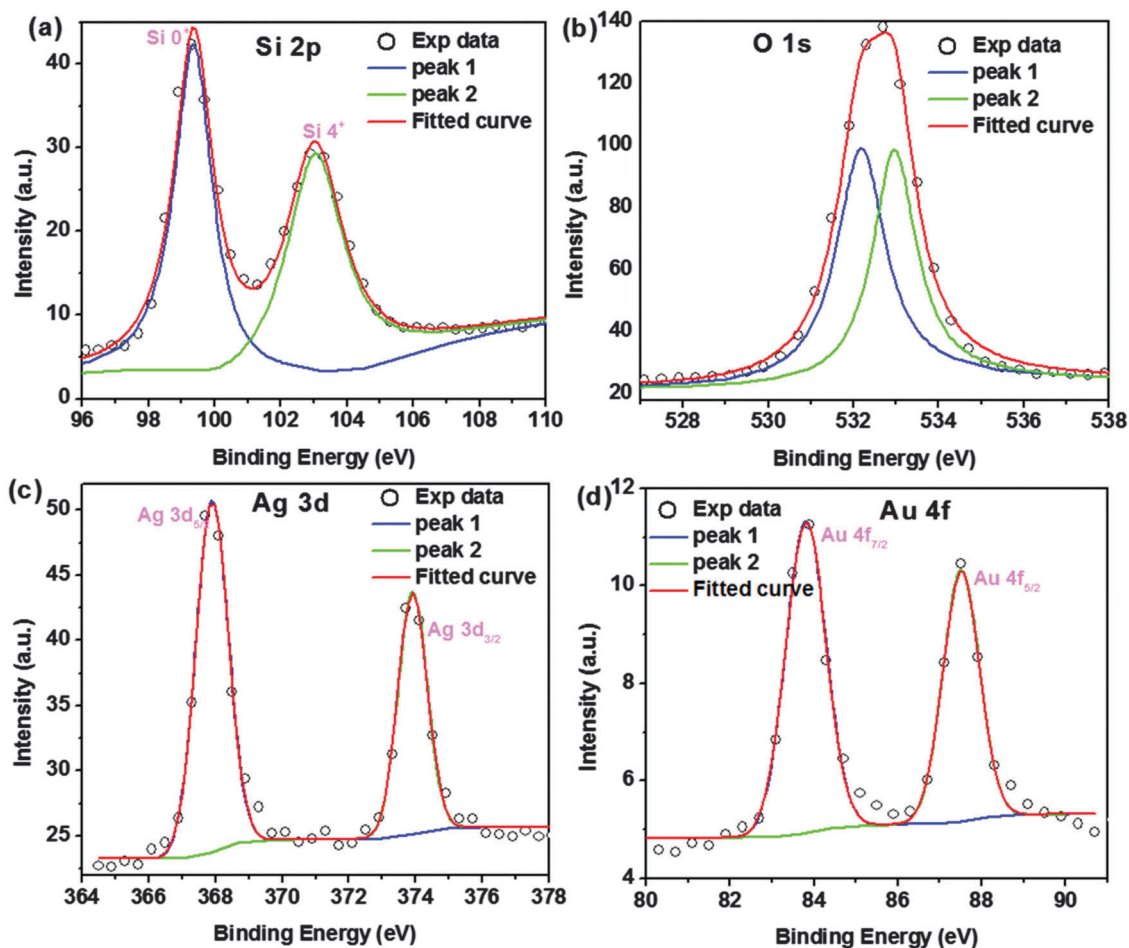


Fig. 2 Core level XPS spectra of AgAuSi: (a) Si 2p; (b) O 1s; (c) Ag 3d and (d) Au 4f. Each curve is fitted with two Gaussian peaks after choosing an appropriate baseline (Shirley).

in Fig. 2(b), the XPS peak at  $\sim 532.7$  eV is attributed to  $O^-$  ions in the Si–O bonds due to the sub-oxide layer of Si, which is consistent with the Si 2p core level spectrum. The asymmetric shape of the O 1s spectrum of AgAuSi in Fig. 2(b) is fitted by choosing the appropriate XPS baseline (Shirley). The peaks at 533.0 eV and 532.2 eV for AgAuSi are assigned to  $O^-$  ions in the  $SiO_2$  bonds and  $O^-$  ions in the oxygen deficient regions, *i.e.*  $Si_2O_3$ , respectively.<sup>38,39</sup> From the XPS compositional analysis, the atomic ratio of oxygen to Si is found to be  $\sim 1.58$ . Fig. 2(a) also confirms that the atomic ratio of oxygen to Si is 1.5 ( $Si_2O_3$ ). This leads to nonbridging oxygen hole center (NBOHC,  $\equiv Si-O^*$ , where, “\*” represents an unpaired hole) defects in the  $SiO_x$  layer. This is consistent with the PL spectra that show defect related emission (discussed later). Fig. 2(c and d) show the Ag 3d and Au 4f XPS core level spectra confirming the presence of Ag and Au NPs in AgAuSi. Despite the post growth etching of Si NWs in  $HNO_3$  solution, Ag and Au NPs reside on the surface and at the bottom of the Si NWs. It was shown from the XPS depth profile that the density of metal NPs increases with depth from the top surface of the Si NWs.<sup>36</sup> These metal NPs influence the PL and photocatalytic properties of the Si NWs/NCs.

### 3.3. Raman and FTIR analysis

Raman studies further confirm the presence of Si NCs on the surface of the Si NWs, which are covered by a thin layer of  $SiO_x$  as well as an amorphous Si layer.<sup>6</sup> Fig. 3(a) depicts a comparison of the first order Raman spectra of AgSi, AuSi and AgAuSi. It is clear that the TO Raman mode of bulk Si at  $\sim 520.5$   $cm^{-1}$  is red-shifted for all the NW samples. However, the red shift ( $\Delta\omega$ ) is different for different samples ( $\Delta\omega_{AgSi} \sim 0.6$   $cm^{-1}$ ,  $\Delta\omega_{AuSi} \sim 1.7$   $cm^{-1}$  and  $\Delta\omega_{AgAuSi} \sim 1.9$   $cm^{-1}$ ). These Raman shifts can be explained on the basis of competing effects of phonon confinement and strain on the NWs.<sup>6,40–42</sup> With the decrease in size from bulk to nanometer, the phonon confinement effect results in the red shift and asymmetrical broadening of the Raman modes. Besides the phonon confinement effect, lattice strain also causes a Raman peak shift ( $\Delta\omega$ ). The  $\Delta\omega$  is positive (blue shift) for compressive strain and negative (red shift) for tensile strain.<sup>6,7,42</sup> Since the red-shift is very small compared to the shift expected from the phonon confinement effect expected from these ultra-small Si NCs,<sup>6</sup> the blue shift expected from the compressive strain due to the  $SiO_x$  layer may be partly compensated by the red-shift due to the phonon confinement effect. Note that the Raman results are consistent with the HRTEM results.

It has been reported that the MACE grown Si NWs are covered by a layer of very small size amorphous Si NCs or Si–H.<sup>6</sup> The surface composition of the samples was characterized by FTIR reflectance analysis and the results are depicted in Fig. 3(b). The FTIR spectra of different samples show the characteristic bending mode at  $\sim 880$   $cm^{-1}$  and asymmetric stretching mode of the Si–O–Si bridge at  $\sim 1,108$   $cm^{-1}$ .<sup>43,44</sup> Further, the peak at  $\sim 613$   $cm^{-1}$  is in general attributed to the Si–H wagging mode, the peak at  $\sim 670$   $cm^{-1}$  is possibly due to the Si–H<sub>2</sub> rolling mode and the peak at  $\sim 960$   $cm^{-1}$  is due to the Si–H<sub>3</sub> bending mode.<sup>43,44</sup> The peak at  $\sim 802$   $cm^{-1}$  is attributed to the Si–OH stretching mode.<sup>43</sup> Here, the Si–H and Si–O–Si bonds strongly

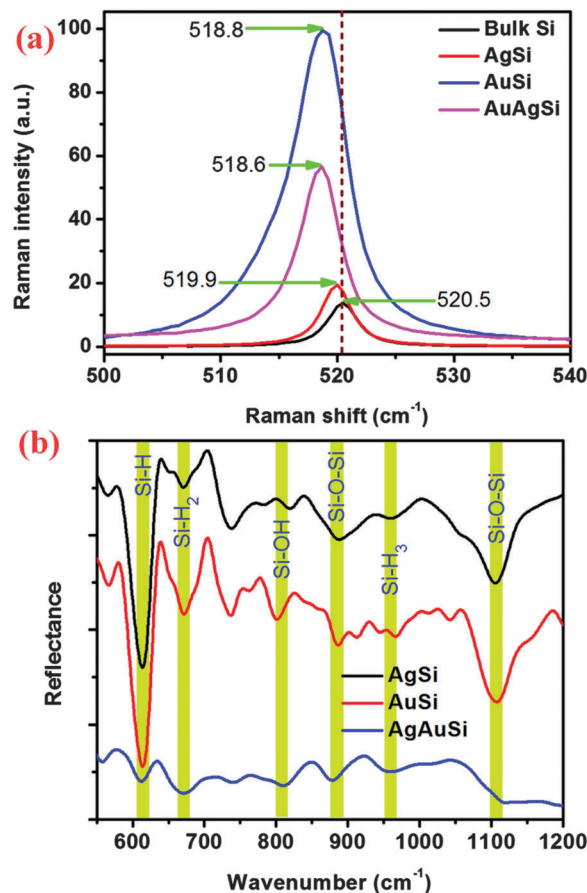


Fig. 3 (a) Comparison of the 1st order Raman spectra for AgSi, AuSi and AgAuSi with that of the bulk Si. The peak centers are denoted in  $cm^{-1}$  unit. (b) Comparison of the FTIR reflectance spectra for AgSi, AuSi and AgAuSi showing different vibrational modes. The green vertical boxes indicate the position of the characteristic modes of Si.

support the fact that the samples are covered by a layer of  $SiO_x$  and amorphous Si–H, which is consistent with the XPS and Raman analyses.

### 3.4. Visible-NIR PL

Si NWs fabricated by MACE usually exhibit broad band PL in the visible region at RT.<sup>7,14,20,30,45</sup> Fig. 4(a) shows the PL spectra of AgSi, AuSi and AgAuSi. The inset shows the PL excitation (PLE) spectrum of AgAuSi with a broad peak centered at 392 nm and the PL spectra were taken with laser excitation of 405 nm for obtaining high PL intensity. Note that the PL intensity of AgAuSi is about two orders of magnitude higher than that of the AgSi and AuSi. The spectra of AgSi and AuSi are scaled up by a factor of 10 to enable comparison. The origin of the strong enhancement of the PL intensity will be discussed later. We note that due to the large diameter and indirect bandgap of the Si NWs, the strong visible PL is unlikely to originate from the Si NW core. On the other hand, the dimensions of the self-grown Si NCs with a broad distribution of sizes are comparable/smaller than the excitonic Bohr diameter ( $\sim 10$  nm) in Si. Therefore, the QC effect of carriers in the Si NCs (average diameter  $< 5$  nm),

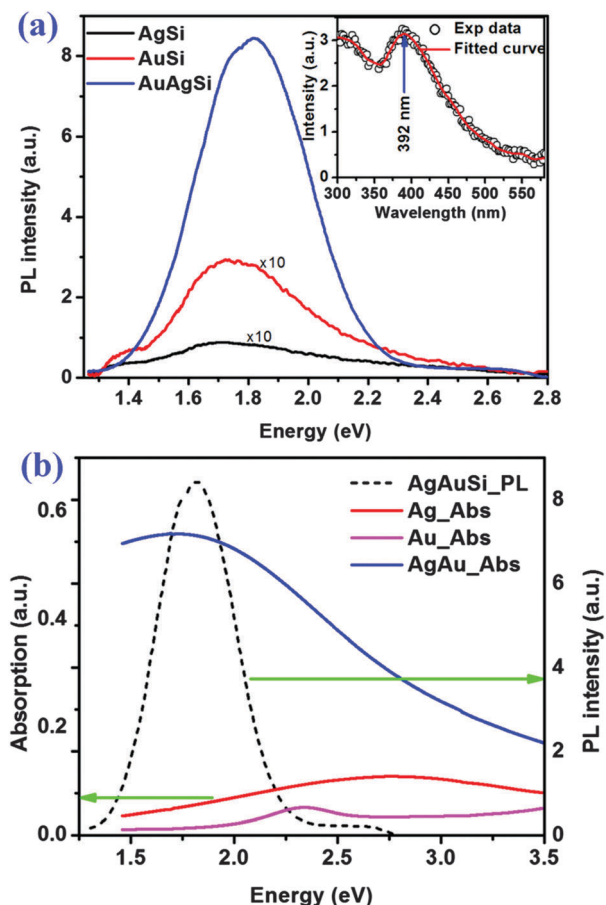


Fig. 4 (a) Comparison of the PL spectra for AgSi, AuSi and AgAuSi. PL spectra of AgSi and AuSi are scaled up by a factor 10 to enable comparison. The inset shows PLE spectrum of AgAuSi exhibiting a distinct absorption peak at 392 nm. (b) Absorption spectra (solid curves) of the Ag film (10 nm), Au film (2 nm) and Ag/Au (10 nm Ag and 2 nm Au) bilayer film on quartz substrates. For comparison, the PL emission spectrum (dashed curve) of AgAuSi is also shown.

instead of that in Si NWs, is most likely responsible for the visible PL shown in Fig. 4(a).<sup>7</sup> In a previous study, we have quantitatively analyzed the PL and Raman spectra of Si NC decorated Si NWs and shown that the visible PL and the Raman shift are primarily contributed by the Si NCs due to the QC effect.<sup>6,7</sup> Note that in the case of Ag/Au bilayer assisted etching, the surface etching of Si NWs is more precise and uniform and this gives rise to well-formed long Si NWs even for short etching duration.<sup>30,31</sup> Due to the large surface area of Si NWs covered with high density of Si NCs, PL emission is strong in AgAuSi as compared to the other samples where the NW growth is incomplete.

It is clear from XPS and EDX analyses that the MACE grown Si NWs have residual metal NPs (Ag, Au) lying at the bottom of the NWs and partly at the surface of the NWs/NCs. Localized surface plasmon resonance (SPR) originating from these metal NPs may enhance the PL intensity of the MACE grown Si NWs.<sup>46</sup> In order to understand the contribution of the SPR effect in the PL spectra, we have measured the absorption spectra of the metal NPs films on a glass substrate. Fig. 4(b) shows the comparison of the absorption spectra of the Ag (10 nm), Au (2 nm) and

Ag/Au bilayer (10 nm Ag followed by 2 nm Au) films on quartz substrates deposited under identical conditions. The PL spectrum of AgAuSi is also plotted together to correlate with the absorption spectra of the metal NPs films. Interestingly, the bilayer film shows about one order of magnitude higher intensity of SPR absorption than the single layer Ag or Au film. It is clear from Fig. 4(b) that the high intensity SPR absorption peak (centered  $\sim 1.75$  eV) of the Au/Ag film has a strong overlap with the PL spectrum of the AgAuSi. The SPR absorption peak for Ag film is at  $\sim 2.7$  eV and for Au film it is at  $\sim 2.35$  eV. The SPR absorption band of AgAu bimetal is red shifted and broad compared to the individual Ag or Au SPR peak. This type of red shift has been reported from Au–Ag alloyed nanoshells and alloyed nanocages with pores on their surfaces, Ag–Au NPs and porous Au NPs.<sup>47,48</sup> In the present case, the initial thickness of Ag and Au layers was chosen such that it forms a discontinuous but interconnected structure on Si wafer. In the case of AgAuSi, the Ag/Au bilayer film may have formed specific nanostructures that showed a broad band and a red shifted SPR band. Since the maximum PL enhancement from the Si NCs may occur in the region of the SPR absorption band of the metal NPs, AgAuSi shows the highest PL intensity with enhancement over a broad wavelength range. This is consistent with the diffused reflectance spectrum of AgAuSi discussed later. We note an enhancement of absorption intensity by a factor of  $\sim 5$  in AgAuSi as compared to AgSi, as shown in Fig. 4(b). However, the PL enhancement factor is much larger (a factor of  $\sim 94$ ), which points to the contributions by other factors such as longer length/high density of Si NWs/NCs, enhanced radiative recombination and increase of the light extraction efficiency due to scattering by metal NPs. Time resolved PL measurements (discussed later) on these samples show much faster PL decay in AgAuSi in comparison to AgSi and AuSi. Note that the broad enhancement can be partly caused by the photon recycling process. The photons emitted from the Si NCs with higher energy can produce other photons with comparatively smaller energy. Thus, the enhanced PL intensity in AgAuSi is partly due to the SPR induced enhanced absorption of the Si NWs/NCs in the presence of AuAg NPs. For Si NCs in a SiO<sub>2</sub> matrix, the highest reported PL intensity enhancement in the presence of nanoscale Ag island arrays was 7-fold,<sup>49</sup> while in the case of Si NWs it was only 4-fold.<sup>20</sup> Huh *et al.*,<sup>50</sup> Patrick *et al.*,<sup>51</sup> and Goffard *et al.*<sup>52</sup> reported enhancements by a factor of 2, 3.9 and 6, respectively, in light emission efficiency from Si NC light-emitting diodes *via* SPR by employing Au NPs. A similar enhancement by a factor of 3 in PL intensity in Si NW/Au NP composites was reported by the Au-catalyzed chemical etching method.<sup>53</sup> The enhancement in PL efficiency was explained in terms of radiative energy exchange between Si NCs and metal NPs due to enhanced radiative coupling of exciton–plasmon.<sup>51,53</sup> In the present case, overall enhancement in PL intensity (by a factor of 94) is remarkable and cannot be fully explained by the SPR effect of the Ag/Au bilayer alone.

In a recent report, we have quantitatively analyzed the origin of the tunable visible PL from MACE grown Si NWs/NCs using a single layer Ag metal as the catalyst and deduced the size dependent bandgap of Si NCs using a QC model.<sup>6,7</sup> From the

heterogeneous relation between the diameter ( $d$ ) of the Si NCs (assuming an equivalent circular cross-section) and corresponding PL peak energy, the bandgap ( $E_g$ ) is inversely proportional to " $d$ ". Note that the porosity of the Si NWs is highly dependent on the concentration of the etching solution. By changing the volume ratio of HF and  $H_2O_2$  the PL behavior of the same bilayer sample (AgAuSi) was monitored. Fig. S2 (ESI $^\dagger$ ) shows a comparison of the visible-NIR PL spectra of AgAuSi grown at different HF: $H_2O_2$  concentrations. It is clear that at higher  $H_2O_2$  concentration, the PL spectra is red shifted and the PL intensity is enhanced. It can be explained by the fact that higher concentration of  $H_2O_2$  makes higher porosity Si NWs, which provides higher density of the Si NCs and it causes enhanced PL intensity. Note that higher porosity also results in smaller size Si NCs that would provide a blue shifted PL peak, instead of a red shift observed here. Therefore, the QC effect alone cannot explain the observed strong visible-NIR PL from bilayer assisted MACE grown Si NWs. The etching mechanism involves the hole injection from metal ions to the underneath Si (in the presence of the oxidant  $H_2O_2$ ) and the  $SiO_2$  dissolution by HF. The dissolution rate is slower when the concentration of HF/ $H_2O_2$  is 2:1 as compared to higher HF concentration cases. As a result, the density of defects in the native oxide layer is different for different concentrations of etchant and it also contributes to the PL intensity (Fig. S2, ESI $^\dagger$ ).

Note that the as-grown Si NWs/NCs here are covered with the oxygen deficient  $SiO_x$  layer. Oxygen vacancies ( $V_O$ ) in the interface between Si and amorphous  $SiO_x$  or NBOHC defects within the  $SiO_x$  matrix in the core-shell Si/ $SiO_x$  nanostructure may also contribute to the observed visible PL.<sup>21,23,24</sup> In order to understand the contributions of different species in the broad visible PL, we have deconvoluted the PL spectrum for each sample. Fig. 5 shows that the broad visible PL spectrum of AgAuSi consists of three peaks centered at 1.74 eV (peak 1), 1.92 eV (peak 2) and 2.50 eV (peak 3). Peak 1 is attributed to the QC effect in the Si NCs.<sup>6,7,13,14</sup> The deep red PL at 1.92 eV (peak 2) is attributed to the NBOHC defects in  $SiO_x$ .<sup>21,23,24</sup> The weak peak 3 in the PL spectrum originates from the  $V_O$  defects in the  $SiO_x$  structure.<sup>54</sup> The deconvoluted PL spectra of AgSi and AuSi are shown in Fig. S3 (ESI $^\dagger$ ) and the fitted parameters are shown in Table S1 (ESI $^\dagger$ ). The resultant visible PL spectrum in each case is determined by the relative contribution and interplay of the above three species. Owing to the large surface area of Si NWs, high density of Si NCs and the NBOHC defects, AgAuSi shows stronger visible PL intensity compared to the other samples where NW growth is incomplete. It may be noted that the PL spectral position and intensity in each case depend on the doping type and doping density of the initial Si wafers. The experiments performed on n-type Si wafers with a lower resistivity of  $0.02 \Omega \text{ cm}^{-1}$  showed red shifted and reduced intensity of PL as compared to that of the p-type higher resistivity ( $10 \Omega \text{ cm}^{-1}$ ) wafer case. This is due to the change in porosity/density of Si NWs/NCs and nonradiative Auger recombination that may reduce the PL efficiency. Defects can also work as the recombination center to decay the excitons.

In order to gain further insight into the origin of PL and its enhancement, we performed dilute HF treatment of AgAuSi in

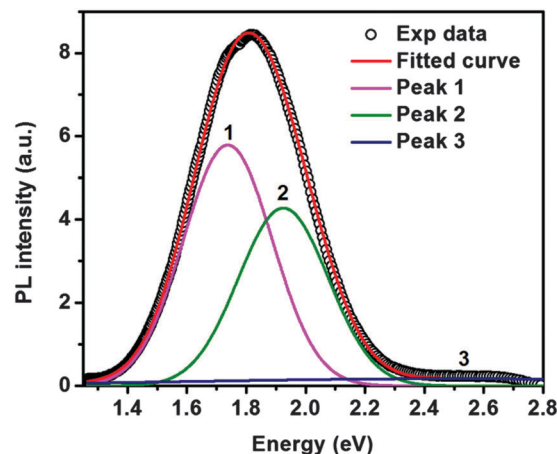


Fig. 5 RT PL spectrum of the AgAuSi fitted with three different Gaussian peaks: peak 1, 2, and 3.

10% HF solution for 30 s (sample code: AgAuSi\_HF) to remove the native oxide layer and performed the PL measurement immediately after etching, under identical conditions. Fig. 6 shows the comparison of the PL spectra of AgAuSi\_HF with the as-grown AgAuSi. Interestingly, there is about one order of magnitude enhancement in the intensity of PL immediately after HF etching. Normalization of the peak intensity reveals no considerable shift in the mean peak position, though the spectral shape is changed to some extent. In order to understand the shape evolution of the PL spectrum after etching, the PL spectrum was fitted with three Gaussian peaks. The fitted curves and fitting parameters are shown in Fig. S4 and Table S1 (ESI $^\dagger$ ), respectively. It is clear that the relative intensity of peak 1 with respect to that of peak 2 is enhanced after HF etching. The intensity ratio of peak 1 to peak 2 is highest in the case of HF etched AgAuSi ( $\sim 2.3$ ), whereas it is  $\sim 1.35$  in as-grown AgAuSi (before HF etching). It is due to the fact that the dilute HF etching partially removes the native oxide layer and reduces the relative contribution of PL due to NBOHC defects in the oxide layer. On the other hand, due to the removal of the  $SiO_x$  layer after HF etching, the contribution of Si NCs to PL is enhanced and this results in enhanced intensity of peak 1 arising from the QC effect. Note that HF treatment may increase the Si-H bonds and it may partly contribute to the PL. The  $SiO_x$  layer may also contain some nonradiative defects which may quench the PL partly and PL is enhanced after partial removal of the nonradiative defects.

In order to ascertain further the contribution of various species in the PL from bilayer assisted MACE grown Si NWs, we monitored the temporal change in PL at an interval of 5 s while illuminating the sample continuously using an excitation laser (405 nm, 5 mW at source) under ambient conditions. Fig. 7(a) shows the temporal decay of PL acquired from AgAuSi\_HF, while the inset shows the variation of PL intensity as a function of time. Fig. 7(b) shows the comparison of normalized PL spectra acquired immediately (0 s) after laser illumination and after 150 s of illumination. Note that the PL spectral shape is changed after prolonged (150 s) exposure to the laser under

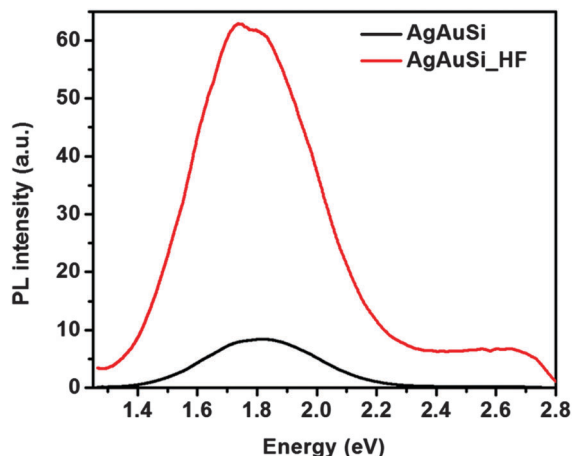


Fig. 6 Comparison of the PL spectra for AgAuSi before and after HF etching. PL intensity is strongly enhanced after HF etching.

ambient conditions. In order to understand the shape evaluation, we have fitted the PL spectra of the sample after 150 s laser exposure. Fig. S5 and Table S1 (ESI<sup>†</sup>) show the fitted curve and fitted parameters, respectively. The fitted curve shows that the intensity of the NBOHC defect related peak ( $\sim 1.9$  eV), *i.e.*, peak 2 is not changed considerably (slightly decreased), though the intensity of peak 1, related to the QC ( $\sim 1.74$  eV) effect, is strongly reduced with laser exposure time. The local heating due to laser may promote local oxidation and create the  $\text{SiO}_x$  layer that may contain nonradiative defects in it and these defects partially quench the PL intensity. This is fully consistent with the results of the post-growth etching experiments discussed above. Note that the surface oxidation may reduce the porosity of Si NWs, which reduces the PL intensity of the Si NCs.<sup>39</sup> As the laser exposure time progresses, the rate of decrease of PL intensity goes down. After a considerable time (150 s), the laser induced local heating reduces the Si-H bond on the H-terminated surface of Si. The Si NCs may be oxidized partially due to the laser induced local heating and the PL arising from the NBOHC defects in the  $\text{SiO}_x$  layer decides the PL spectral line shape. In our earlier work,<sup>7</sup> it was shown that nonradiative defects contribute to PL mainly at low temperature ( $< 200$  K). TRPL data at room temperature (discussed below) show that the NBOHC defect related PL decay rate is much faster than the intrinsic PL from Si NCs/NWs. Thus, the contribution of the specific type of defect (*e.g.* NBOHC) in the visible PL is significant in the present case.

In order to understand the effect of laser heating on the PL spectra, the PL measurements were performed at different excitation powers ranging from 5 to 100 mW (at source). Fig. 8 shows the comparison of the PL spectra of AgAuSi with 405 nm laser excitation at different excitation powers. The inset shows the variation of the peak intensity with excitation power. Again, in this case the shape of the PL spectra is changed at higher laser power. Note that the intensity of the PL spectra increases sub-linearly with increasing laser power (at source) and it reaches a kind of saturation at high power (100 mW). This is mainly due to the laser induced heating that partially removes

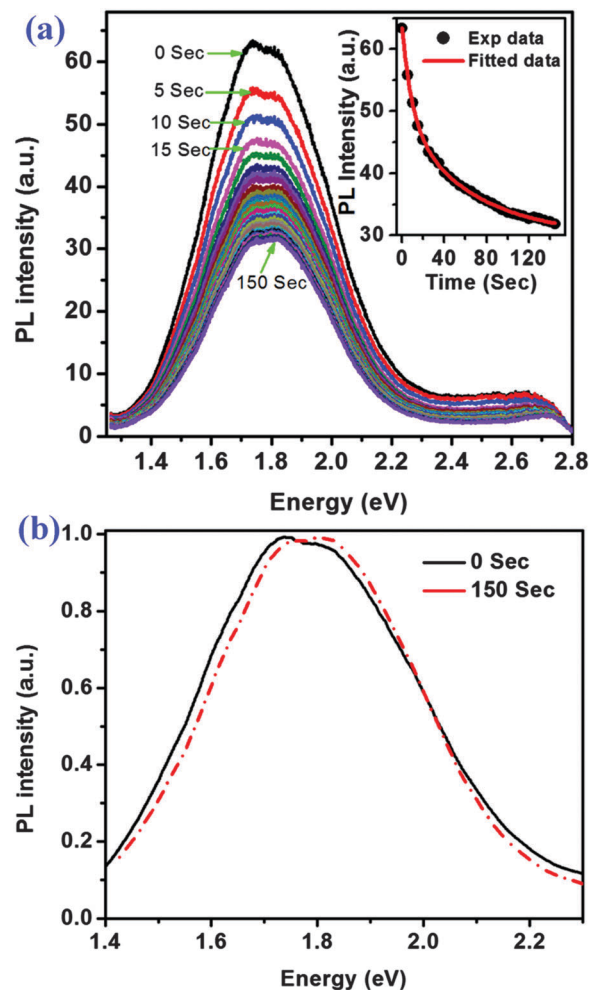


Fig. 7 (a) Time evolution of the PL spectra of HF etched AgAuSi acquired under ambient conditions at an interval of 5 s. The inset shows the intensity of PL as a function of time,  $t$  (laser illumination) and the fitted data points show a bi-exponential decay. (b) The normalized PL spectra of AgAuSi\_HF immediately ( $t = 0$  s) after laser exposure and after 150 s laser illumination.

the Si-H bonds and oxidizes the Si NWs due to ambient conditions.<sup>39</sup> Due to a thicker oxide layer, PL intensity is reduced. This is consistent with the results of HF etching induced changes in PL intensity. Thus, the strong PL from the MACE grown Si NCs/NWs arises from the QC of carriers in Si NCs as well from NBOHC defects in the  $\text{SiO}_x$  layer. Since the PL intensity is relatively high in our samples, an estimate of the relative quantum yield (QY) of the samples was made taking rhodamine 6G (R6G) as the standard reference.<sup>55</sup> Note that the Si NW/NCs samples are in the form of films, where the measurement of the quantum yield is difficult. Taking the standard QY of R6G in water as 92%, the estimated values of QY are 0.009%, 0.013% and 0.104% for the samples AgSi, AuSi and AgAuSi, respectively. The QY of the sample AgAuSi is 11.5 and 8 times higher than that of the AgSi and AuSi samples, respectively. It may be noted that the measured QYs of the Si NW/NC films are much smaller than that reported for dense Si NCs embedded in the  $\text{SiO}_2$  matrix, which are measured in solution.<sup>56</sup>

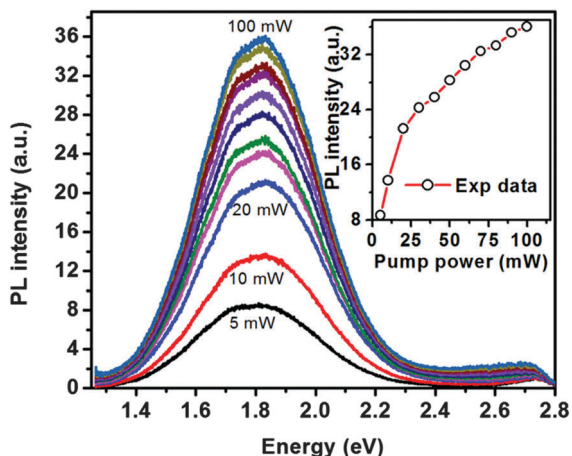


Fig. 8 Excitation power dependent PL spectra of AgAuSi. The inset shows the PL peak intensity as a function of laser power (at source).

### 3.5. Time resolved PL

Time resolved PL studies were undertaken to ascertain the contribution of different species in the PL decay of the Si NWs/NCs. Fig. 9(a) shows the comparison of the decay of PL intensity as a function of time for AgSi, AuSi and AgAuSi monitored at emission energy 1.91 eV. Each decay curve could be fitted well with a bi-exponential decay with time constants in the range of a few ns. The fitting parameters are shown in the inset in Fig. 9(a). Due to the contribution of two distinct species with different time constants of decay ( $\tau_1$ ,  $\tau_2$ ), the PL decay fits to a bi-exponential function. The slower component ( $\tau_1$ ) is attributed to the QC effect and the faster component  $\tau_2$  is attributed to the NBOHC defects. Note that there is a considerable reduction in  $\tau_1$  as well as  $\tau_2$  for AgAuSi as compared to that of AgSi or AuSi. It has been reported that the radiative emission rate of Si NCs is increased after Au incorporation.<sup>52</sup> In the present case, Ag/Au NPs are present on the surface of the Si NCs attached with the Si NWs. These metal NPs can accelerate the radiative recombination rate of Si NCs. This might be partly responsible for the high intensity of PL in AgAuSi. To understand the contribution of two different species in the PL decay of AgAuSi, we have studied the PL decay properties monitored at different emission energies ( $E_m$ ) and the results are shown in Fig. S6 (ESI<sup>†</sup>). Each curve is fitted by a bi-exponential decay and the fitted parameters are tabulated in the inset. It can be seen from the fitting parameters that the  $\tau_1$  decreases at higher  $E_m$ , while  $\tau_2$  increases at higher  $E_m$ . Thus, the two components show opposite trends. This confirms that two components of PL have different origins, consistent with the steady state PL data. Earlier reports suggest the  $\tau_{\text{eff}}$  would decrease with the increase in  $E_m$  due to the QC effect.<sup>57</sup> Since  $\tau_1$  follows the trend expected from the QC effect,  $\tau_1$  is attributed to the PL decay due to the QC effect. Note that at 2.26 eV, PL decay reaches the base level, while it does not reach base level for PL at 1.77 eV. This is consistent with the steady state PL data that show negligible contribution of the PL peak at 1.74 eV to the PL decay at 2.26 eV. Thus, it can be concluded that the broad visible-NIR PL from the AgAuSi arises from the combined effect of QC in Si NCs and

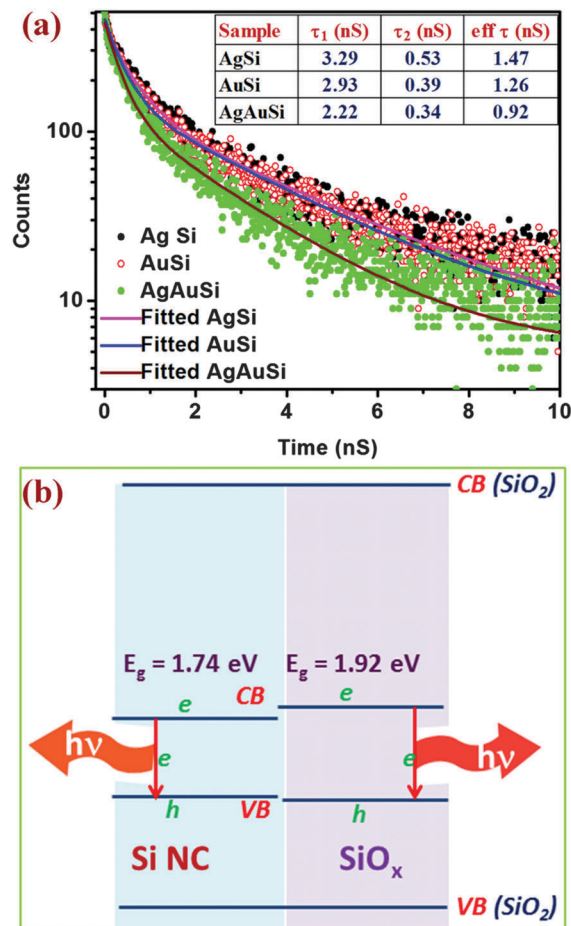


Fig. 9 (a) Comparison of the TRPL decay for AgSi, AuSi and AgAuSi monitored at 1.91 eV. Each curve is fitted by a bi-exponential decay and the fitted parameters are tabulated in the inset. (b) A schematic energy band diagram showing the different PL components originating from Si NCs and defects in  $\text{SiO}_x$ . "VB" and "CB" refer to valence and conduction bands, respectively.

the NBOHC defects in  $\text{SiO}_x$  structure. The TRPL data strongly suggest that the radiative recombination rate is enhanced in the case of AgAuSi as compared to the case of AgSi or AuSi. This is partly responsible for the enhanced PL in AgAuSi. Fig. 9(b) shows a schematic of the band diagram showing the contributions of Si NCs and NBOHC defects in the  $\text{SiO}_x$  layer to the observed visible-NIR PL from the bilayer assisted MACE grown Si NWs/NCs.<sup>58</sup> Note that the PL is strongly enhanced due to the higher density of Si NW/NCs, stronger absorption aided by SPR enhancement and the enhanced radiative recombination rate caused by the Ag/Au NPs on the Si NCs.

### 3.6. Optical reflectivity

In order to better understand the relative intensity of PL for different samples, absorption coefficient of the Si NWs/NCs was assessed by measuring the diffused reflectivity of the samples under oblique incidence. Fig. 10 shows a comparison of the diffused reflectivity as a function of energy for the bulk Si wafer and different Si NWs/NCs. Interestingly, AgAuSi shows the

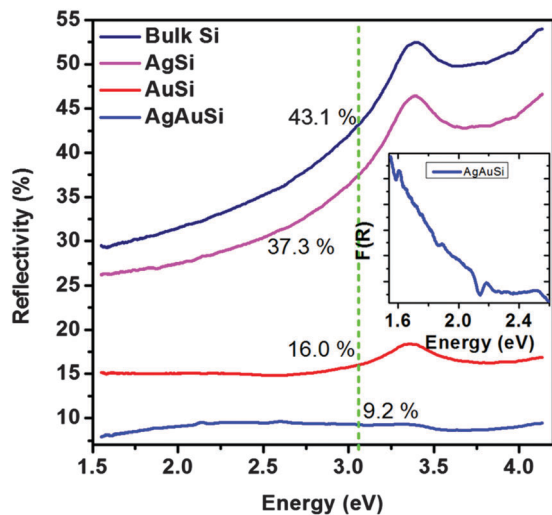


Fig. 10 Comparison of the diffused reflectance spectra for AgSi, AuSi and AgAuSi with that of the bulk Si wafer. The dotted vertical line shows the reflectivity of the respective samples at a wavelength of 405 nm. The inset shows the Kubelka–Munk absorption function  $F(R)$  for AgAuSi showing strong absorption in the range 1.55–2.09 eV.

lowest reflectivity (9.1% at 405 nm) among all samples indicating the strongest absorption that may be partly responsible for the enhanced visible PL intensity from AgAuSi compared to AgSi and AuSi. Due to multiple reflections on the inner surface of the Si NWs and enhanced absorption by the Si NCs (sizes <5 nm) with a broad range of size distribution, the absorption is significantly high over the entire range of wavelength in AgAuSi. The inset of Fig. 10 shows the plot of Kubelka–Munk function  $F(R)$  as a function of energy for AgAuSi in the visible region. It shows strong absorption in the range 1.55–2.09 eV, which is partly due to the SPR enhancement of the bimetal NPs and it is consistent with the UV-vis absorption of the bimetal NPs on quartz, as discussed in Fig. 4(b). A comparison of  $F(R)$  for AgSi and AgAuSi shows much higher absorption in AgAuSi.<sup>20</sup> Thus, higher PL intensity is partly caused by the higher absorption of AgAuSi. Higher absorption implies more efficient excitation of carriers finally leading to enhanced radiative recombination or PL in AgAuSi. Ultra low reflectivity of the Si NWs in AgAuSi is extremely beneficial for high efficiency solar photovoltaic devices.

### 3.7. Visible light photocatalysis

The excitons generated within the nanoporous Si NWs could be energetic enough to drive applicable photoelectrochemical reactions due to their wide range of optical absorption with high intensity and broad visible emission centered near the red region. Fig. 11(a) shows a comparison of the photocatalytic degradation efficiency of MB for AgSi, AuSi, AgAuSi and bulk Si wafer under visible light illumination for 1 h. The inset shows the photo-degradation efficiency of AgAuSi as a function of time. In this case, a small piece (0.8 cm<sup>2</sup>) of sample containing Si NWs/NCs was put in a beaker containing 25 ml of MB solution and it was exposed to visible light (390–720 nm) for different durations (up to 200 min) using a programmable Xe lamp (250 W).

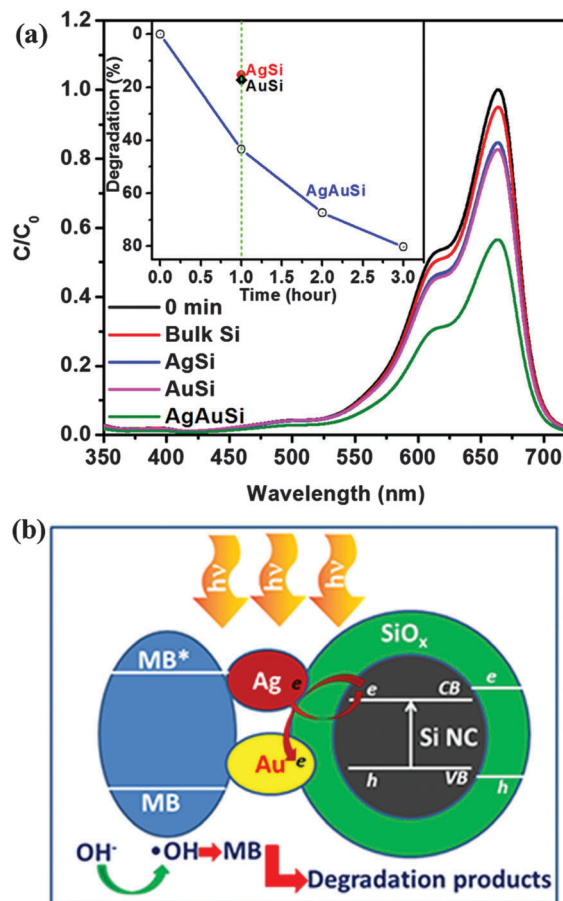


Fig. 11 (a) Comparison of the photo-degradation of MB by AgSi, AuSi and AgAuSi with that of the bulk Si wafer under 1 h visible light illumination. The inset shows the photo-degradation efficiency of AgAuSi as a function of illumination time. Corresponding degradation values for AgSi and AuSi after 1 h are also shown (filled circle and square). (b) The schematic illustration of the photocatalytic activity of the Ag/Au bilayer assisted MACE grown Si NWs/NCs.

When a photon with energy equal to or greater than the band gap of the Si NWs/NCs reaches the catalyst's surface, it results in the generation of an electron in the conduction band and a hole in the valence band. The induced hole receives the electron from adsorbed water and results in  $\bullet\text{OH}$  free radical groups.<sup>25,26</sup> Fig. 11(b) shows the schematic diagram of the photocatalytic activity of the Si NWs/NCs grown by Ag/Au bilayer assisted MACE. FTIR spectra confirm that the Si–H bonds are present in the Si NC/NW structure and XPS spectra along with PL analysis confirm that the SiO<sub>x</sub> layer contains NBOHC defects. The terminated hydrogen in Si–H and oxygen in Si–O (NBOHC defects) are electron-deficient and may serve as an electron sink and hence accelerate the separation of photoinduced e–h pairs, which promotes the photocatalytic activity of the Si NWs/NCs. Finally, the reactive  $\bullet\text{OH}$  radicals oxidize and degrade MB by collapsing the chain of the organic molecule.<sup>25,26</sup> This leads to high degradation of MB with AgAuSi. Kang et al reported photocatalytic activity of size controlled Si quantum dots (Si QDs) that exhibited tunable emission in the near-infrared to blue

wavelength region.<sup>28</sup> It is believed that the H-terminated Si NCs covered by Si sub-oxide is possibly the best Si based photocatalyst compared to the other Si structure (bulk Si and Si nanostructure). In the present case, AgAuSi shows the highest photodegradation ( $\sim 43\%$  in 1 h) of MB compared to that of AgSi ( $\sim 15\%$ ) or AuSi ( $\sim 18\%$ ). It is clear that the aspect ratio of the Si NWs is highest for AgAuSi as compared to the other samples. Due to the large surface area of Si NWs covered with high density of Si NCs, the density of Si-H is high in AgAuSi as compared to the other samples where NW growth is incomplete and this is believed to give rise to efficient photocatalysis by AgAuSi. Note that the metal NPs (Ag, Au and Ag/Au) present within pores between the Si NWs and on the surface of the Si NCs can enhance the photocatalytic activity. Because of the differences in their Fermi levels, it can introduce a Schottky barrier between the metal NPs and Si NWs/NCs. The built-in potential at the Schottky diode junction can facilitate the efficient separation of photogenerated e-h pairs and influence the degradation of the dye strongly. Furthermore, the electronegativity of Au is higher than that of Ag or Si. Hence, the Au or Ag/Au bilayer can accelerate the separation of photoinduced e-h pairs better, which can increase the photocatalytic activity of the nanoporous Si NWs (Fig. 11).<sup>25,27</sup> It is clear from Fig. 10 that the AgAuSi possesses ultralow reflectance, *i.e.*, very high absorption over the entire visible range. The results clearly demonstrate that the Ag/Au bilayer assisted grown Si NWs are much more efficient photocatalysts than the Ag or Au assisted grown Si NWs. Furthermore, the Ag/Au NPs show SPR related broad visible absorption (Fig. 4 and 10) and these metal NPs can also function as the catalysts to facilitate certain redox reactions to degrade the organic pollutants.<sup>26</sup> This could also contribute to the enhanced photocatalytic activity in the case of bilayer assisted MACE grown Si NWs. Note that in the present experiment, we used a small piece of Si NW/NCs sample compared to the total volume of the MB dye. If a bigger size of sample is used, higher efficiency degradation can be achieved from AgAuSi. In order to compare the efficiency of degradation of AgAuSi with the industry standard photocatalyst P25 (TiO<sub>2</sub>), we have prepared a thin film of P25 by drop casting on the same size Si wafers (same as that of AgAuSi) and compared the efficiency, as shown in Fig. S7(a) (ESI<sup>†</sup>). It is clear that the photocatalytic nature of the Ag/Au bilayer MACE grown Si NWs is quite comparable to the best known standard photocatalyst, P25. Note that the photocatalysis efficiency depends on the ionic conditions of the dye as well as the sample. In the present study, Si-H primarily takes part in the photocatalysis, which is anionic in nature. If the dye is cationic (such as MB) then the rate is higher compared to the anionic dye (such as Methyl Orange (MO)). We have measured the photodegradation efficiency in MO as well and compared it with that of MB, as shown in Fig. S7(b), (ESI<sup>†</sup>). As expected, the rate is slower in the case of MO.

It is interesting to note that AgAuSi shows highly efficient PL as well as improved photocatalysis under visible light. The PL process requires a fast radiative recombination of the excited e-h pairs, while the photocatalysis requires an easy separation of the photoexcited e-h pairs with minimum recombination.

Surprisingly, these two contrasting phenomena are simultaneously present in the same material reported here. Anpo *et al.* reported PL and photocatalytic activity of highly dispersed TiO<sub>2</sub> anchored onto porous vycor glass.<sup>59</sup> Yin *et al.* reported the enhanced visible PL and strong photocatalytic activity of V<sub>2</sub>O<sub>5</sub>-loaded ZnO nanorods (NRs) and attributed them to the coupling between ZnO NRs and V<sub>2</sub>O<sub>5</sub> NPs.<sup>60</sup> A similar type of coupling may be expected in the Si NCs and metal NP system. We have taken the PL spectra of AgAuSi after the photocatalysis experiment *i.e.*, visible light illumination (for 3 hour) in MB solution. Fig. S8(a) (ESI<sup>†</sup>) shows the comparison of the PL spectra for AgAuSi before and after the photodegradation experiment. The inset shows the PL spectrum of pristine MB on Si wafers. Fig. S8(b) (ESI<sup>†</sup>) shows the PL spectrum of AgAuSi\_MB fitted with four different Gaussian peaks originating from different sources. It is clear that the PL intensity is not changed considerably after light exposure. The peak centers as well as the intensities of peak 1 and peak 2 are not changed considerably, while the intensity of the V<sub>O</sub> related peak, *i.e.*, peak 3 is enhanced after light exposure. This is possibly due to the thick oxide layer formed on Si NWs/NCs after photodegradation. The results of FTIR analysis before and after photocatalysis are shown in Fig. S9(a and b) (ESI<sup>†</sup>). It is clear that the vibrational modes associated with the H-terminated surface of Si are eliminated after the photocatalysis. Our Raman results in Fig. S9(c) (ESI<sup>†</sup>) also confirm that the stretching modes of Si-H bonds in Si NWs are reduced after photocatalysis.<sup>61</sup> It has been reported that the H-terminated surface is mostly responsible for the excellent photocatalytic activity of the MACE grown Si NWs.<sup>25,27</sup> We believe that the SPR absorption and increased radiative recombination in the Ag/Au bilayer metal NP decorated Si NWs/NCs are primarily responsible for the efficient PL, while the H-terminated surface and the Schottky barrier between the metal NPs and the Si NWs/NCs are primarily responsible for the efficient photocatalysis in the bilayer assisted MACE grown Si NWs. It is also likely that two different regions of the metal NP decorated Si NWs/NCs may take part in the two different processes. Note that the large surface area and defects in the nanoporous Si NWs are beneficial for the photocatalysis process, as reported for the porous ZnO nanosheets.<sup>62</sup> More studies may be needed to pinpoint the exact mechanism. These results demonstrate the superiority of bilayer assisted etching for the growth of multifunctional Si NWs and open up the possibility of using the MACE grown Si NW arrays for light emitting diodes, solar cells, organic waste treatment and hydrogen production by photocatalytic water splitting *etc.*

## 4. Conclusions

We reported on the benefit of using Ag/Au bimetal over the conventional single Ag or Au metal layer as a catalyst for the MACE growth of Si NWs/NCs in terms of improved morphology and superior optoelectronic properties. As compared to the case of single metal assisted etching, bimetal assisted etched Si NWs/NCs exhibited about two orders of magnitude enhancement in the visible-NIR PL. It is shown that the broad band and

tunable visible-NIR PL originates from the combined effect of QC in Si NCs and the NBOHC defects in the SiO<sub>x</sub> layer. Our conclusions are strongly supported by the Raman, XPS and FTIR analyses. The bimetal assisted MACE grown Si NWs/NCs show extremely low reflectance in the entire visible-NIR region and thus are highly promising for photovoltaic applications. The enhanced PL is attributed to the longer length/higher density of the Si NWs/NCs, higher density of NBOHC defects, SPR enhanced absorption and the enhanced radiative decay rate due to the presence of the bimetallic NPs. Si NWs grown by MACE exhibit excellent photocatalytic degradation of MB under visible light due to the presence of the H-terminated surface. The bimetal catalyst MACE grown Si NWs show higher photocatalytic degradation of MB as compared to the conventional Ag or Au assisted growth case and it is believed to arise from the higher density of the Si-H terminated surface and the process of carrier separation is aided by the Schottky barrier effect due to the presence of metal NPs. These results are very promising for various light emitting and photocatalytic applications of MACE grown Si NWs. The superiority of bilayer assisted grown Si NWs can be exploited in various cutting edge applications, e.g., Si based optoelectronics, environmental cleaning, etc.

## Acknowledgements

We acknowledge the financial support from CSIR (Grant No. 03(1270)/13/EMR-II), DEITY (Grant No. 5(9)/2012-NANO(VOL-II)) and BRNS (Grant No. 2012/37P/1/BRNS) for carrying out part of this work. Part of this work was supported by JSPS invitation fellowship (2012) to PKG. Central Instruments Facility, I.I.T. Guwahati is acknowledged for the HRTEM, FESEM and Raman facilities.

## References

- 1 B. Tian, X. Zheng, T. J. Kempa, Y. Fang, N. Yu, G. Yu, J. Huang and C. M. Lieber, *Nature*, 2007, **449**, 885.
- 2 R. Yan, D. Gargas and P. Yang, *Nat. Photonics*, 2009, **3**, 569.
- 3 K.-Q. Peng and S.-T. Lee, *Adv. Mater.*, 2011, **23**, 198.
- 4 K. Peng, J. Jie, W. Zhang and S. T. Lee, *Appl. Phys. Lett.*, 2008, **93**, 033105.
- 5 Z. Li, Y. Chen, X. Li, T. I. Kamins, K. Nauka and R. S. Williams, *Nano Lett.*, 2004, **4**, 245.
- 6 R. Ghosh, A. Pal and P. K. Giri, *J. Raman Spectrosc.*, 2015, **46**, 624.
- 7 R. Ghosh, P. K. Giri, K. Imakita and M. Fujii, *Nanotechnology*, 2014, **25**, 045703.
- 8 L. T. Canham, *Appl. Phys. Lett.*, 1990, **57**, 1046.
- 9 M. V. Wolkin, J. Jorne, P. M. Fauchet, G. Allan and C. Delerue, *Phys. Rev. Lett.*, 1999, **82**, 197.
- 10 L. E. Brus, P. F. Szajowski, W. L. Wilson, T. D. Harris, S. Schuppler and P. H. Citrin, *J. Am. Chem. Soc.*, 1995, **117**, 2915.
- 11 N. A. Hill and K. B. Whaley, *Phys. Rev. Lett.*, 1995, **75**, 1130.
- 12 M. Ehbrecht, B. Kohn, F. Huisken, M. A. Laguna and V. Paillard, *Phys. Rev. B: Condens. Matter Mater. Phys.*, 1997, **56**, 6958.
- 13 G. Ledoux, J. Gong, F. Huisken, O. Guillois and C. Reynaud, *Appl. Phys. Lett.*, 2002, **80**, 4834.
- 14 A. S. Kuznetsov, T. Shimizu, S. N. Kuznetsov, A. V. Klekachev, S. Shingubara, J. Vanacken and V. V. Moshchalkov, *Nanotechnology*, 2012, **23**, 475709.
- 15 T. Matsumoto, J. I. Suzuki, M. Ohnuma, Y. Kanemitsu and Y. Masumoto, *Phys. Rev. B: Condens. Matter Mater. Phys.*, 2001, **63**, 195322.
- 16 O. Demichel, F. Oehler, P. Noé, V. Calvo, N. Pauc, P. Gentile, T. Baron, D. Peyrade and N. Magnea, *Appl. Phys. Lett.*, 2008, **93**, 213104.
- 17 O. Demichel, V. Calvo, P. Noé, B. Salem, P. F. Fazzini, N. Pauc, F. Oehler, P. Gentile and N. Magnea, *Phys. Rev. B: Condens. Matter Mater. Phys.*, 2011, **83**, 245443.
- 18 K. Kusova, L. Ondič, E. Klimesova, K. Herynkova, I. Pelant, S. Danis, J. Valenta, M. Gallart, M. Ziegler, B. Honerlage and P. Gilliot, *Appl. Phys. Lett.*, 2012, **101**, 143101.
- 19 A. G. Cullis, L. T. Canham and P. D. J. Calcott, *J. Appl. Phys.*, 1997, **82**, 909.
- 20 W. Chern, K. Hsu, I. S. Chun, B. P. D. Azeredo, N. Ahmed, K. H. Kim, J.-m. Zuo, N. Fang, P. Ferreira and X. Li, *Nano Lett.*, 2010, **10**, 1582.
- 21 S. S. Walavalkar, C. E. Hofmann, A. P. Homyk, M. D. Henry, H. A. Atwater and A. Scherer, *Nano Lett.*, 2010, **10**, 4423.
- 22 A. R. Guichard, R. D. Kekatpure, M. L. Brongersma and T. I. Kamins, *Phys. Rev. B: Condens. Matter Mater. Phys.*, 2008, **78**, 235422.
- 23 T. Suzuki, L. Skuja, K. Kajihara, M. Hirano, T. Kamiya and H. Hosono, *Phys. Rev. Lett.*, 2003, **90**, 186404.
- 24 L. Skuja, T. Suzuki and K. Tanimura, *Phys. Rev. B: Condens. Matter Mater. Phys.*, 1995, **52**, 15208.
- 25 M. Shao, L. Cheng, X. Zhang, D. D. D. Ma and S. T. Lee, *J. Am. Chem. Soc.*, 2009, **131**, 17738.
- 26 Y. Qu, X. Zhong, Y. Li, L. Liao, Y. Huangbe and X. Duan, *J. Mater. Chem.*, 2010, **20**, 3590.
- 27 N. Megouda, Y. Cofinier, S. Szunerits, T. Hadjersi, O. ElKechai and R. Boukherroub, *Chem. Commun.*, 2011, **47**, 991.
- 28 Z. Kang, C. H. A. Tsang, N. B. Wong, Z. Zhang and S.-T. Lee, *J. Am. Chem. Soc.*, 2007, **129**, 12090.
- 29 K. Q. Peng, Y. J. Yan, S. P. Gao and J. Zhu, *Adv. Mater.*, 2002, **14**, 1164.
- 30 Y. Qu, H. Zhoua and X. Duan, *Nanoscale*, 2011, **3**, 4060.
- 31 J. Kim, H. Han, Y. H. Kim, S. H. Choi, J. C. Kim and W. Lee, *ACS Nano*, 2011, **5**, 3222.
- 32 E. G. Barbagioanni, L. V. Goncharova and P. J. Simpson, *Phys. Rev. B: Condens. Matter Mater. Phys.*, 2011, **83**, 035112.
- 33 A. Pal, R. Ghosh and P. K. Giri, *Appl. Phys. Lett.*, 2015, **107**, 072104.
- 34 A. I. Hochbaum, D. Gargas, Y. J. Hwang and P. Yang, *Nano Lett.*, 2009, **9**, 3550.
- 35 S. M. Kim and D. Y. Khang, *Small*, 2014, **10**, 3761.
- 36 R. Ghosh, P. K. Giri, K. Imakita and M. Fujii, *J. Alloys Compd.*, 2015, **638**, 419.
- 37 S. Kim, M. C. Kim, S. H. Choi, K. J. Kim, H. N. Hwang and C. C. Hwang, *Appl. Phys. Lett.*, 2007, **91**, 103113.
- 38 G. M. Bancroft, H. W. Nesbitt, R. Ho, D. M. Shaw, J. S. Tse and M. C. Biesinger, *Phys. Rev. B: Condens. Matter Mater. Phys.*, 2009, **80**, 075405.

- 39 Y. R. Choi, M. Zheng, F. Bai, J. Liu, E. Tok, Z. Huang and C.-H. Sow, *Sci. Rep.*, 2014, **4**, 4940.
- 40 A. Shchepetov, M. Prunnila, F. Alzina, L. Schneider, J. Cuffe, H. Jiang, E. I. Kauppinen, C. M. S. Torres and J. Ahopelto, *Appl. Phys. Lett.*, 2013, **102**, 192108.
- 41 C. M. Hessel, J. Wei, D. Reid, H. Fujii, M. C. Downer and B. A. Korgel, *J. Phys. Chem. Lett.*, 2012, **3**, 1089.
- 42 Y. Chen, B. Peng and B. Wang, *J. Phys. Chem. C*, 2007, **111**, 5855.
- 43 W. J. Salcedo, F. J. R. Fernandez and E. Galeazzo, *Braz. J. Phys.*, 1997, **27**, 158.
- 44 K. Fobelets, C. B. Li, D. Coquillat, P. Arcade and F. Teppe, *RSC Adv.*, 2013, **3**, 4434.
- 45 A. Najjar, A. B. Slimane, M. N. Hedhili, D. Anjum and R. Sougrat, *J. Appl. Phys.*, 2012, **112**, 033502.
- 46 E. Mulazimoglu, G. Nogay, R. Turan and H. Emrah Unalan, *Appl. Phys. Lett.*, 2013, **103**, 143124.
- 47 Y. Sun and Y. Xia, *J. Am. Chem. Soc.*, 2004, **126**, 3892.
- 48 D. Mott, N. T. B. Thuy, Y. Aoki and S. Maenosono, *Philos. Trans. R. Soc., A*, 2010, **368**, 4275.
- 49 J. S. Biteen, N. S. Lewis, H. A. Atwater, H. Mertens and A. Polman, *Appl. Phys. Lett.*, 2006, **88**, 131109.
- 50 C. Huh, C.-J. Choi, W. Kim, B. Kyu Kim, B.-J. Park, E. H. Jang, S.-H. Kim and G. Yong Sung, *Appl. Phys. Lett.*, 2012, **100**, 181108.
- 51 K. Potrick and F. Huisken, *Phys. Rev. B: Condens. Matter Mater. Phys.*, 2015, **91**, 125306.
- 52 J. Goffard, D. Gérard, P. Miska, A.-L. Baudrion, R. Deturche and J. Plain, *Sci. Rep.*, 2013, **3**, 2672.
- 53 M. Bassu, M. L. Strambini, G. Barillaro and F. Fuso, *Appl. Phys. Lett.*, 2010, **97**, 143113.
- 54 L. Tsybeskov, J. V. Vandyshv and P. M. Fauchet, *Phys. Rev. B: Condens. Matter Mater. Phys.*, 1994, **49**, 7821.
- 55 M. Brouwer Albert, *Pure Appl. Chem.*, 2011, **83**, 2213.
- 56 R. J. Walters, J. Kalkman, A. Polman, H. A. Atwater and M. J. A. de Dood, *Phys. Rev. B: Condens. Matter Mater. Phys.*, 2006, **73**, 132302.
- 57 A. M. Hartel, S. Gutsch, D. Hiller and M. Zacharias, *Phys. Rev. B: Condens. Matter Mater. Phys.*, 2013, **87**, 035428.
- 58 S. Dhara, C. Y. Lu, K. G. M. Nair, K. H. Chen, C. P. Chen, Y. F. Huang, C. David, L. C. Chen and R. Baldev, *Nanotechnology*, 2008, **19**, 395401.
- 59 M. Anpo, N. Aikawa, Y. Kubokawa, M. Che, C. Louis and E. Giamello, *J. Phys. Chem.*, 1985, **89**, 5017.
- 60 H. Yin, K. Yu, J. Hu, C. Song, B. Guo, Z. Wang and Z. Zhu, *Dalton Trans.*, 2015, **44**, 4671.
- 61 M. H. Brodsky, M. Cardona and J. J. Cuomo, *Phys. Rev. B: Solid State*, 1977, **16**, 3556.
- 62 D. Liu, Y. Lv, M. Zhang, Y. Liu, Y. Zhu, R. Zong and Y. Zhu, *J. Mater. Chem. A*, 2014, **2**, 15377.